Temperature-dependent dynamics of NH3-derived Cu species in the Cu-CHA SCR catalyst

Temperature-dependent dynamics of NH_3-derived Cu species in the Cu-CHA SCR catalyst

Elisa Borfecchia[a]*, Chiara Negri[a], Kirill A. Lomachenko[b], Carlo Lamberti[c,d], Ton V. W. Janssens[e], Gloria Berlier[a]

Department of Chemistry, NIS Centre and INSTM Reference Center, University of Turin, Via Giuria 7, Turin, 10125 Italy.

European Synchrotron Radiation Facility, 71 avenue des Martyrs, CS 40220, Grenoble Cedex 9, 38043 France.

International Research Institute "Smart Materials", Southern Federal University, Zorge str. 5, Rostov-on-Don, 344090 Russia.

Department of Physics, CrisDi Centre and INSTM Reference Center, University of Turin, Via Giuria 1, Turin, 10125 Italy.

Umicore Denmark ApS, Nøjsomhedsvej 20, Kgs. Lyngby, 2800 Denmark.

Abstract

The Cu-exchanged CHA zeolite (Cu-CHA) is a promising catalyst for the NH_3-assisted selective catalytic reduction (NH_3-SCR) of harmful nitrogen oxides (NO_x, x = 1, 2), combining high hydrothermal stability with a good performance in the 200-550 °C range. Despite many recent breakthroughs in the molecular-scale understanding of this catalyst, several open questions remain to ultimately unravel the NH_3-SCR mechanism across the operation-relevant temperature range. In this context, we apply *in situ* XAS and UV-Vis-NIR spectroscopy to assess the nature and thermal stability of NH_3-derived Cu-species in a commercial Cu-CHA deNO_x catalyst. Both techniques evidence a fast and complete 'solvation' by NH_3 of the framework-coordinated Cu^{II} and Cu^{I} ions formed upon thermal activation of the catalyst. Our results confirm that NH_3 desorption at T > 200 °C is accompanied by $Cu^{II} \rightarrow Cu^{I}$ reduction phenomena, while the compresence of pre-adsorbed NH_3 with gas-phase NO greatly enhances the reduction rate and efficiency. By applying state-of-the-art Multivariate Curve Resolution (MCR) analysis, we elaborate these insights in a quantitative picture of Cu-speciation during NH_3 temperature-programmed desorption (TPD) and surface reaction (TPSR) experiments. MCR analysis confirms recent theoretical predictions for the thermal stability of $[Cu^{I}(NH_3)_2]^+$ species and allows us to experimentally identify the framework-coordinated O_{fw}-Cu^{I}-NH_3 intermediate formed upon desorption of a NH_3 ligand from $[Cu^{I}(NH_3)_2]^+$.

1. Introduction

The road transport sector is one of the driving forces of EU economy and a key factor for keeping dynamic cities and urban networks, but it also represents one of the major air pollution sources, being the largest contributor to NO_x emissions (39 % in the EU-28).[1]. This represents a serious threat to human health (with related important costs for the EU economy) notwithstanding the strict *Euro 6* regulations introduced in recent years (2014), which prescribe 80% reduction in NO_x emissions.[2] A significant R&D activity has thus been focused in the last two decades to the development of stable and active catalysts to reduce NO_x emission from diesel exhaust aftertreatment systems.[3] Metal exchanged zeolites have been readily identified for such application by the scientific community. However, the real breakthrough came from the discovery of the small pore chabazite framework (Cu-CHA) catalysts, which combine high hydrothermal stability with a good performance in the 200-550 °C range.[4, 5]

Cu ions, introduced in Cu-CHA by ion exchange as Cu^{II}, are able to reversibly change their oxidation state depending on activation conditions and presence of reactants.[6, 7] In oxidizing conditions both $Z[Cu^{II}(OH)]$ and Z_2Cu^{II} species (where Z indicates a framework negative charge induced by the presence of framework Al atoms) are formed, with relative concentration depending on the sample Cu/Al and Si/Al ratios.[8, 9] The possible presence of $Z[Cu^{II}OO^{\bullet}]$ species was also recently put forward.[7, 10, 11] On the other hand, in inert/reducing conditions, ZCu^{I} sites can be stabilized in 6- or 8-member rings (6MR and 8MR).[6, 12]

The NH_3-SCR reaction can be divided into two half-cycles. In the reduction part, Cu^{II} ions are readily converted into Cu^{I} in the presence of NO and NH_3, releasing the reaction products, N_2 and H_2O. The crucial step of the cycle is believed to be the re-oxidation of Cu^{I} to Cu^{II}, involving the activation of O_2,[8, 13-16] which is promoted by the presence of NO.[15] Most of the current literature is focused on this kinetically relevant half-cycle. For instance, Janssens et al. proposed copper(II) nitrates formed upon interaction of the catalyst with NO + O_2 as an important

intermediate of the cycle.[13, 17, 18] The role of nitrates was debated by Marberger et al. on the basis of time-resolved X-ray absorption spectroscopy (XAS) experiments,[16] while other authors proposed the relevance of the nitrosonium ion NO^+,[19] of a 'nitrite route[20]' and of ammonium nitrate.[21] A different point of view concerning the O_2 activation step was recently proposed by Paolucci et al.,[14] who highlighted the crucial role of the mobile $[Cu^I(NH_3)_2]^+$ complexes formed upon interaction at 200 °C of Cu^{II} ions with the NO+NH_3 mixture.[13, 22, 23] The different kinetic regimes measured by many research groups on samples with high and low Cu loadings were thus explained by assuming the formation of active $Cu^I(NH_3)_2$-O_2-$Cu^I(NH_3)_2$ pairs, which are favoured at Cu density above 0.2 Cu/1000 Å^3.[14] The effect of Al distribution on this mechanism has been also assessed by *ab initio* molecular dynamics simulations.[24]

Notwithstanding the importance of the re-oxidation step, many aspects of the chemistry taking place during the reduction half-cycle are still under investigation.[22, 25-27] As mentioned above, mobile $[Cu^I(NH_3)_2]^+$ species are known to be present in NH_3-SCR conditions at low reaction temperatures,[13, 22, 23] together with a fraction of ammonia-solvated Cu^{II} ions. These could be in the form of $[Cu^{II}(NH_3)_4]^{2+}$[13, 23] or include an OH^- ligand resulting in $[Cu^{II}(NH_3)_3(OH)]^+$ complexes.[8] Notice that the discrimination between these two species is not straightforward with most characterization techniques. For instance XAS, which is one of the most powerful technique to give a precise description of the metal ion coordination sphere, cannot precisely discriminate between O and N ligands.[23] On the other hand, the $[Cu^I(NH_3)_2]^+$ species, which are supposed to play a crucial role in the oxidation step, has been shown to be unstable above 250 °C in NH_3-SCR conditions, resulting in a significant fraction of framework-coordinated Cu^{II} ions.[23] Thus, the reactivity of NH_3 in Cu-CHA still presents interesting scientific aspects. For instance, Lezcano-Gonzales et al. showed that NH_3 is also adsorbed on extra-framework Al species, and, importantly, ammonia is stored in the form of ammonium ions NH_4^+, by reaction with residual (not-exchanged) Brønsted sites.[22] Very recently, Chen et al.[27] used first principle calculations to propose a molecular level interpretation of NH_3-TPD measurements, supporting the presence of $[Cu^{II}(NH_3)_3(OH)]^+$ species contributing to the two NH_3-TPD peaks observed below 200 °C and in the 250-350 °C range for Cu-CHA catalysts.[28-30]

This work is thus set in the scientific discussion focused on the reduction half-cycle, concerning the reactivity of NH_3 with Cu-CHA. The reduction of Cu^{II} to Cu^I, forming the mobile $[Cu^I(NH_3)_2]^+$, is almost complete at 200 °C in the presence of NO + NH_3, while exposure to NH_3 alone results in a mixture of NH_3-solvated Cu^{II} and Cu^I ions.[13] This indicates that NH_3 alone can act as a reducing agent, but not as efficient as the NO + NH_3 combination. Starting from this observation, we explored the formation, thermal stability and reactivity of amino-complexes by *in situ* XAS and Diffuse Reflectance UV-Vis-NIR (DR-UV-Vis-NIR) spectroscopy under different conditions. Namely, XAS measurements were carried out during NH_3-TPD experiments starting from Cu-CHA samples activated in oxidizing or inert conditions, that is starting from Cu^{II} or Cu^I ions, respectively (e1 and e2). Temperature Programmed Surface Reaction (TPSR) of the Cu-amino complexes formed on an O_2-activated sample was also followed in the presence of NO (experiment e3). The NH_3 interaction and subsequent desorption/surface reaction was studied from 100 to 500 °C, to obtain information on the low temperature reactivity of ammonia, and on the stability of Cu-amino complexes during the NH_3-TPD process. Moreover, Multivariate Curve Resolution (MCR) analysis[31-33] was applied to extract the X-ray absorption near edge structure (XANES) signatures of the involved Cu-species.[9, 10] This allowed us to propose structural models of the involved species and decomposition intermediates, and to follow quantitatively their evolution as a function of temperature, catalyst pre-treatment and reaction atmosphere.

2. Experimental

2.1 Catalyst synthesis and compositional characteristics

The Cu-CHA zeolite (SSZ-13) catalyst investigated in this work was synthesized and characterized as described in our previous reports.[6, 34, 35] The material has Cu/Al = 0.444 and Si/Al = 13.1, as determined by ICP-OES elemental analysis. As shown in previous works, the activated catalyst mostly contains redox-active $Z[Cu^{II}(OH)]$ species,[6, 12, 36, 37] charge-balanced at isolated *1Al* exchange sites. Z_2Cu^{II} species, at paired *2Al* exchange sites in 6MR are

expected to represent a minor component (10-20% total Cu, depending on the specific pre-treatment conditions adopted), in line with the composition-dependent trends highlighted in the recent literature.[7-9]

2.2 *In situ* XAS

2.2.1 Gas flow setup and conditions for *in situ* XAS experiments. *In situ* XAS experiments were carried out on the BM23 beamline[38] of the European Synchrotron Radiation Facility (ESRF) using the Microtomo reactor cell,[39] developed by the ESRF sample environment group. The Cu-CHA powder, in its hydrated form at RT in air, was pressed in a self-supporting wafer with mass optimized for XAS measurements in transmission mode (~ 100 mg, resulting in $\Delta\mu x = 0.5$ with total absorption after the edge of $\mu x = 2.5$) and fixed inside the reactor cell. The cell was connected to an *ad hoc* gas flow setup, consisting of three main channels, each of them connected with stainless steel tubes to gas bottles with different composition, namely pure He, pure O_2 and 1% NO/He. The total flow rate and the composition of the feed were adjusted by three mass flow controllers. The cell was also connected to a *vacuum* line installed on the beamline. Such setup was necessary for the fast switching from flow to static configuration. After stopping the flow, it allowed evacuating the cell volume down to 10^{-4} mbar pressure by means of a turbomolecular pump, as well as dosing NH_3 to the sample in static conditions. The sample temperature during *in situ* experiments was controlled by the heating system integrated in the Microtomo cell.

In this work, we performed three *in situ* XAS experiments, herein referred to as e1, e2 and e3. The corresponding temperature profile and gaseous environment at the sample are schemed in Figure 1. In e1, the sample was activated at 400 °C (heating ramp 3 °C/min), and maintained at fixed temperature for ca. 60 min. The activation was performed by flowing in the Microtomo cell 100 ml/min 50% O_2/He (O_2-activation). The sample was subsequently cooled to 100 °C (10 °C/min) while keeping the same atmosphere as for the activation. Once the 100 °C temperature was reached, 50 mbar of pure NH_3 were dosed to the sample from the *vacuum* line (after switching the cell inlet to the *vacuum* line channel) and kept interacting with the catalyst for 10 min. The sample was subsequently flushed with 100 ml/min of He under isothermal conditions at 100 °C and monitored by time-dependent XAS data until no further changes were observed in the XANES. The final step of the experiment consisted in NH_3-TPD conducted in He from 100 to 500 °C (heating rate 5 °C/min). The catalyst was kept at 500 °C in the same TPD atmosphere until the XAS signal was stabilized. Experiment e2 was conducted under the same conditions as e1, but the catalyst was activated to 400 °C in *vacuum* (*vacuum*-activation). Experiment e3 was conducted as e1 (O_2-activation) but NH_3-TPD was replaced by TPSR in 1% NO/He.

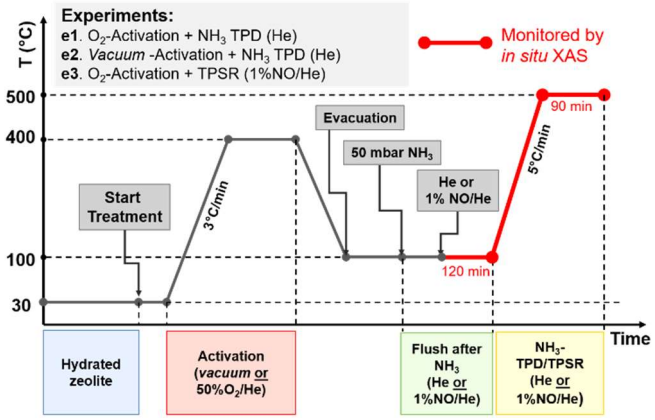

Figure 1. Schematic representation of the experimental conditions (temperature profiles and gaseous atmosphere) for the three *in situ* XAS experiments e1 (O_2-activation + NH_3-TPD), e2 (*vacuum*-activation + NH_3-TPD), e3 (O_2-activation + TPSR). Please note that the horizontal experiment time axis is not in real scale, for graphical reasons.

2.2.2 XAS data acquisition and data reduction procedures. *In situ* Cu K-edge XAS were collected in transmission mode, using double-crystal Si(111) monochromator for the incident energy scan and ionization chambers to detect incident (I_0) and transmitted photons (I_1). A Cu foil was measured simultaneously with all the collected XAS spectra by means of a third ionization chamber (I_2), for energy calibration.[40, 41] The chambers were filled with a He/Ar mixture up to 2.2 bar with Ar partial pressure of 0.1 and 0.3 bar for I_0 and $I_{1,2}$ chambers, respectively. We monitored the evolution of the XAS signal as a function of time/temperature with faster

acquisitions of ~6 min/scan (during the isothermal step at 100 °C) and 12 min/scan (during TPD/TPSR from 100 to 500 °C). Spectra were collected with a constant energy step in the XANES region (ΔE = 0.5 eV for 6-min scans and 0.3 eV for 12-min ones) and with a uniform sampling step in k-space (Δk = 0.05 $Å^{-1}$). The static states of the catalyst, reached after complete stabilization of the XAS signal at fixed temperature were probed by two consecutive higher-quality XAS scans (~40 min/scan), collected with a sampling step of ΔE = 0.3 eV in the XANES region and Δk = 0.035 $Å^{-1}$ in the EXAFS part. The data were collected up to 13 $Å^{-1}$ with acquisition time increasing quadratically with k from 1 to 4 s/point. For the data analysis, the $\mu(E)$ curves of these two scans were averaged.

All the acquired XAS scans were aligned using their respective Cu metal foil spectra detected by the I_2 ionization chamber. Normalization to unity edge jump and extraction of the $\chi(k)$ functions for the static scans were performed employing the Athena software from the Demeter package.[42] Fourier-transformed (FT-) EXAFS spectra were obtained from the k^2-weighted data in the 2.4 – 12.4 $Å^{-1}$ k-range.

2.2.3 Cu K-edge XANES spectra of model systems and key spectroscopic fingerprints. Focusing on the interaction of Cu-CHA with NH_3, we initially adopted the $[Cu^{II}(NH_3)_4]^{2+}$ and $[Cu^{I}(NH_3)_2]^{+}$ complexes measured in aqueous solution as model systems for NH_3-solvated Cu^{II} and Cu^{I} species (green and red lines, respectively in Figure 2a,c). To guide the interpretation of *in situ* experiments, we also considered the dehydrated states of the catalyst, as characterized after O_2-activation and *vacuum* activation at 400 °C (blue and grey lines, respectively, in Figure 2a,c). For these model spectra, the principal XANES fingerprints of relevant Cu^{I} and Cu^{II} species are highlighted by coloured rectangles in Figure 2a.[6, 43-46]

These include: (i) the weak dipole-forbidden pre-edge peak at ca. 8977 eV, arising from the 1s → 3d transition in d^9 Cu^{II} ions, which unambiguously fingerprints the presence of Cu^{II} in the sample; (ii) the rising-edge peaks in the 8980–8985 eV range, assigned to 1s → 4p transitions in Cu^{I} centres,[47, 48] showing high intensity for linear Cu^{I} species such as the $[Cu^{I}(NH_3)_2]^{+}$ complex in Figure 2a;[35, 49] (iii) the rising-edge peaks in the 8985–8990 eV range, assigned to 1s → 4p transitions in both Cu^{I} and Cu^{II} centres; (iv) the so-called 'white-line' peak (first resonance after the edge), centred around 9000 eV, which intensity is usually directly proportional to the first-shell coordination number.

2.2.4 XANES Linear Combination Fit (LCF) analysis of activated catalyst. Due to the difficulty in obtaining appropriate experimental references to model the XAS of Cu^{I} and Cu^{II} species coordinated to the specific zeolite lattice, MCR-derived reference spectra are a viable alternative, which allow for an accurate quantification of Cu-speciation in activated Cu-zeolites.[7, 9-11, 50] To this aim, we exploited the results obtained in a previous study,[9] where we employed the MCR approach [31-33] to extract the XANES signatures of well-defined Cu-species present in Cu-CHA catalysts with different composition (Cu/Al and Si/Al in the 0.1–0.6 and 5–29 ranges, respectively, synthesized with equivalent approaches as adopted for the Cu-CHA catalyst studied in this work) along the dehydration process. Once these curves have been obtained from the MCR-analysis and attributed to the chemical species on the basis of calculated XANES spectra from DFT-optimized model clusters, they can be employed as references spectra in a simple LCF model to investigate related systems[9, 10, 51, 52] In particular, we considered the MCR-derived curves for the five Cu-species illustrated in Figure 4a, namely hydrated Cu^{II}, under-coordinated hydrated Cu^{II}, $Z[Cu^{II}(OH)]$, Z_2Cu^{II} and ZCu^{I} species. For a detailed discussion on the exact nature of the identified Cu-species, as well as on the limitations of the method in discriminating structurally-similar moieties (e.g. under-coordinated hydrated Cu^{II} with mixed $O_{fw}/OH_2/OH^-$ ligands, or Z_2Cu^{II} formed in correspondence of different Al siting in the zeolite lattice), the interested reader is referred to the original work.[9]

The experimental XANES, $\mu^{exp}(E)$, collected after O_2- and *vacuum*-activation at 400 °C were fitted as linear combinations of the five reference spectra, $\mu^{ref}_i(E)$, *i.e.*: $\mu^{LCF}(E) = \Sigma_i w_i \mu^{ref}_{,i}(E)$, optimizing the weights w_i for each MCR-derived reference spectrum, imposing $0 \leq w_i \leq 1$ and $\Sigma_i w_i = 1$.

XANES LCF analysis was performed using an in-house script written in Wolfram Mathematica environment. After appropriate instructions for importing/interpolating experimental and reference curves, the linear combination fit is performed through the following code:

*"lcf=NonlinearModelFit[exp,{w1*IntR1[x]+w2*IntR2[x]+w3*IntR3[x]+w4*IntR4[x]+w5*IntR5[x],1>=w1>=0, 1>=w2>=0,1>=w3>=0,1>=w4>=0,1>=w5>=0,w1+w2+w3+w4+w5==1},{w1,w2,w3,w4,w5},x];"*

where: *lcf* = linear combination fit curve; *exp* = experimental spectrum; *IntRi[x]* = interpolated reference spectra; *wi*: LCF weight for each interpolated reference spectra *IntRi.*

2.2.5 XANES MCR analysis of *in situ* XAS after interaction with NH_3. MCR analysis of *in situ* XAS data was performed employing the Graphical User Interface (GUI) developed by Jaumot and co-workers,[32] based on the MCR-Alternating Least Squares (MCR-ALS) algorithm,[53] using Matlab R2011b. The analysis was performed simultaneously on the whole *in situ* XAS dataset collected in e1-e3 (globally 59 XANES scans). Here, Principal Component Analysis (PCA) indicated four Principal Components (PCs), based on the evaluation of the scree plot and of the abstract components (scores) for the dataset. The experimental spectra were analysed in the (8972−9022) eV energy range, resulting in 71 energy points. Initial spectra of the four PCs for the ALS routine were guessed by using the purest variable detection method (SIMPLISMA algorithm[54]). 'Soft' constrains employed in the reconstruction included non-negativity for both pure spectra and concentration profiles and closure to 1 for concentration profiles (allowed due to the element selectivity of the XAS technique, probing only and all the Cu-species present in the sample). The MCR-ALS routine converged successfully after 47 interactions. A series of quality indicators for the MCR analysis are reported in Table 1.

Table 1. Quality indicators for the MCR-ALS analysis (4 PCs) of the *in situ* XAS dataset

MCR-ALS Quality Indicator	Value
Std. Dev. of residual vs exp. data	0.0040
Fitting error (LOF) in (%) of PCA	0.2199
Fitting error (LOF) in (%) of exp.	0.5318
Percentage of variance explained at the optimum	99.9972

2.3 In situ Diffuse Reflectance UV-Vis-NIR spectroscopy

The *in situ* UV-Vis-NIR spectra were recorded in the 2500-200 nm range (4000-50000 cm^{-1}) at 1 nm resolution (corresponding to 250 and 1.6 cm^{-1} at 50000 and 4000 cm^{-1}, respectively) on a Varian Cary 5000 spectrophotometer, equipped with a R928 PMT UV-Vis detector and a cooled PbS photocell NIR detector. Spectra were collected with a Praying Mantis® element, coupled with a low temperature (LT) reaction chamber. The sample was pelletized using a hydraulic press, successively crushed and sieved, and the fraction between 300 and 150 μm was selected for the measurement. The background was measured at room temperature (RT) using Teflon powder inserted in the same cell used for the measurements. Measurements were carried out from RT to 400 °C, flowing the desired gases with an *ad hoc* built gas flow set-up. The setup consisted of three channels, each of them connected to a specific gas bottle (pure He, pure O_2, 1.8% NH_3/He) and to a mass flow controller. The lines that lead to the reactor were heated to 130 °C to prevent water vapour or NH_3 condensation.

The sample has been activated in pure O_2 to 400 °C (50 ml/min, heating ramp 5°C/min) and maintained at 400 °C for 60 min. Successively, the temperature was lowered to 200 °C, keeping the O_2 atmosphere, to prevent Cu self-reduction. Once reached the desired temperature, the sample was exposed to 1200 ppm NH_3/He (50 ml/min). The evolution of the system was followed until stabilization and subsequently during heating to 400 °C (heating ramp 5 °C/min) in the same gas feed. A single UV-Vis-NIR spectrum collection required 5 min; consecutive spectra correspond to a temperature increase of ΔT = 25 °C. Spectra are reported as relative reflectance (R%), defined as:

$$R_{\%} = R_{sample}/R_{reference} \times 100$$

3. Results and discussion

3.1 Qualitative insights from in situ XAS

Figure 2 shows an overview of the results at key stages during experiments e1-e3, together with selected reference spectra helpful to guide the interpretation of the *in situ* XAS data.

Cu K-edge XANES (Figure 2a,b) provides a wealth of fingerprints useful to identify oxidation state and coordination geometry of Cu ions.[41, 55, 56] These can be readily interpreted based on several previous studies on Cu-zeolite catalysts, carried out in the context of both NH_3-SCR[8, 13, 16, 17, 23, 49, 57] and methane-to-methanol conversion[7, 10, 58-61] A summary of the relevant spectroscopic fingerprints can be found in Section 2.2.3.

A first observation is that, after interaction of the catalyst with NH_3 at 100 °C and stabilization in He or 1%NO/He, a substantial fraction of the Cu exists in the form of linear Cu^I species, as indicated by the characteristic XANES peak at 8983 eV (Figure 2b). The absence of a well-defined second-shell peak in the FT-EXAFS (Figure 2d) is consistent with the formation of mobile Cu-species. Indeed, Single scattering paths involving the Al/Si atoms of the zeolite closer to the Cu centre lead to a well-defined second-shell peak in the FT-EXAFS spectra (grey shaded box in the 2.0-2.7 Å range in Figure 2c), which then indicates a coordination of the Cu to the zeolite framework.

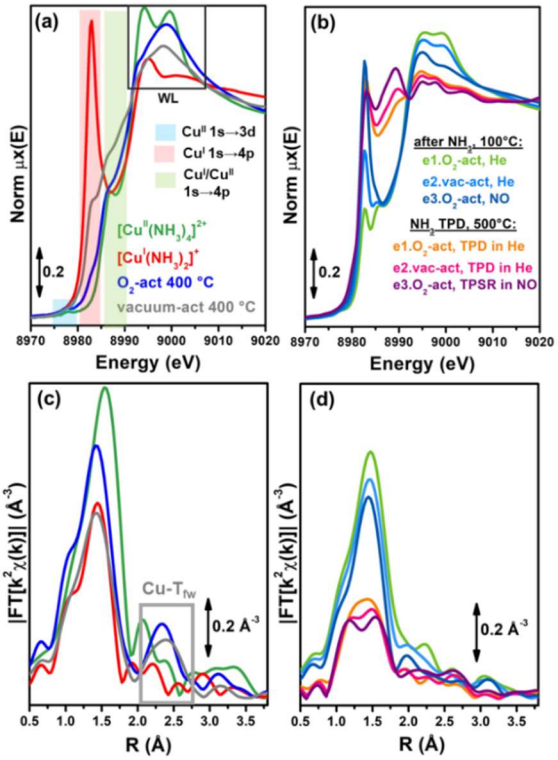

Figure 2. (a) Selected Cu K-edge XANES spectra of model Cu-species or catalyst states, including the $[Cu^{II}(NH_3)_4]^{2+}$ and the $[Cu^{I}(NH_3)_2]^{+}$ complexes and the O_2-activated and *vacuum*-activated state of the Cu-CHA catalyst. The characteristic XANES fingerprints of Cu^I and Cu^{II} species are highlighted by coloured rectangles and summarized in Section 2.2.3. (b) XANES spectra of Cu-CHA at key stages during experiments e1-e3. (c, d) As parts (a) and (b), respectively, but reporting the corresponding the k^2-weighted phase-uncorrected FT-EXAFS spectra, using the same colour code. The grey box in part (c) highlights the R-space region characteristic of Al/Si atoms (T_{fw}) scattering contributions.

It is worth to highlight that a suppressed intensity of the EXAFS signal could be also caused by high structural and thermal disorder affecting framework-coordinated species (becoming especially important at T > 400 °C for Cu^I ions)[62], as well as antiphase effects due to their characteristic coordination environment.[6, 9] However, the similarity between XANES and EXAFS for Cu-CHA after interaction with NH_3 at 100 °C and the reference spectra for the $[Cu^{II}(NH_3)_4]^{2+}$ and $[Cu^{I}(NH_3)_2]^{+}$ complexes strongly support Cu mobilization, in this case.

This is also in line with the recent theoretical study by Chen et al.,[27] which reports that NH_3-TPR experiments should be interpreted considering the NH_3 desorption energy from mobile Cu-amino complexes, rather than from framework-coordinated cations.

A second consideration concerns the Cu^I/Cu^{II} ratio upon stabilization after NH_3 adsorption at 100 °C, as a function of the different experimental conditions adopted in e1-e3. The intensity of the XANES Cu^I fingerprint peak at 8983 eV, which is an indication for the Cu^I fraction in the catalyst, follows the order: e1 < e2 < e3 (green, light blue and

blue curves, respectively, in Figure 2b). Both the activation procedure and the presence of NO after NH_3 adsorption influence the average Cu oxidation state observed.

A higher abundance of framework-coordinated Cu^I species prior to NH_3 adsorption, as a consequence of the thermal treatment in *vacuum,*[9, 35] favours the formation of NH_3-solvated Cu^I species. Moreover, the presence of NO largely enhances the abundance of Cu^I species under comparable temperature and interaction times [8, 13, 63]. Based on the qualitative comparison with the reference XANES spectrum in Figure 2a, most of the Cu occurs as $[Cu^I(NH_3)_2]^+$ species after 120 min from NH_3 adsorption in 1%NO/He already at 100 °C.

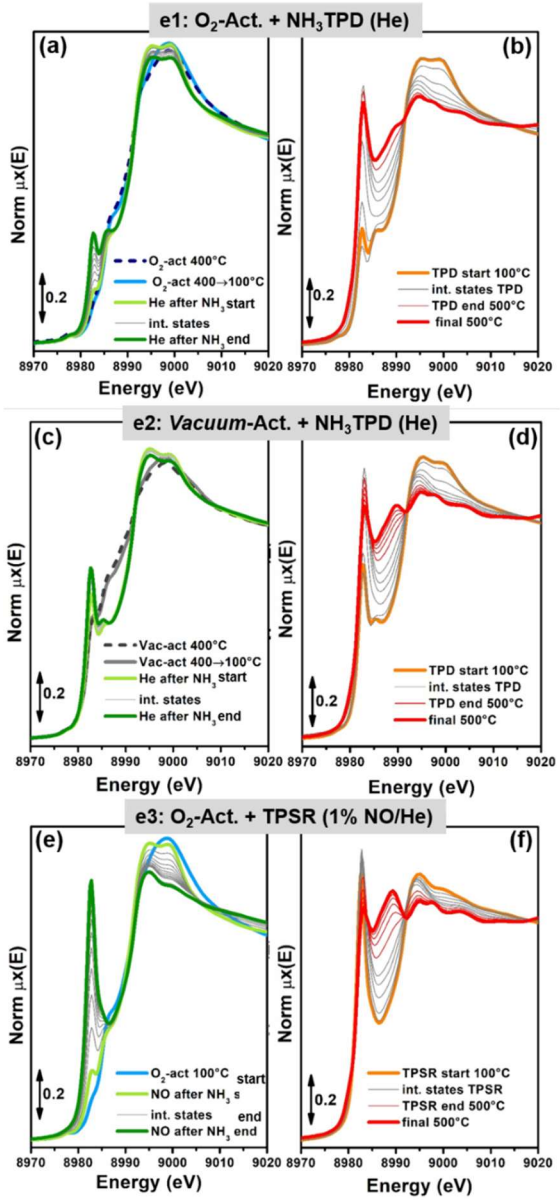

Figure 3. Time-resolved Cu K-edge XANES spectra collected during experiment e1 (a, b), e2 (c, d) and e3 (e, f) as a function of time after interaction with NH_3 at 100 °C (left panels) and as a function of temperature/time during and after TPD (in He, e1 and e2) or TPSR (in 1% NO/He, e3) up to 500 °C (right panels). For comparison, parts (a) and (b) also report the XANES collected on the O_2- and *vacuum*-activated catalyst (dashed dark blue and dark grey lines, respectively) after cooling to 100 °C in the activation atmosphere and, in the case of e1, switching to *vacuum* prior to NH_3 dosage.

Figure 2b,d also compares the final XAS spectra of the catalysts after TPD/TPSR at 500 °C. Under these conditions, the Cu appears to be reduced to Cu^I for all the three experiments.

Nonetheless, from the qualitative analysis of the XANES, it is clear that a different Cu^I species is formed, characterized by a rising-edge peak at 8983 eV broader and less intense with respect to the one observed for linear

$[Cu^{I}(NH_3)_2]^+$, as well as by a prominent resonance at 8989 eV. The trend in the intensity of the characteristic XANES features among the three experiments is the same observed as at 100 °C, with the most developed features observed in e3, in the presence of NO. The corresponding FT-EXAFS spectra (Figure 2d) show a broadened and dampened first-shell peak, while it is impossible to distinguish well-defined contributions at higher distance from the Cu-absorber. High temperature data collection (500 °C) causes an inherent damping of the EXAFS signal. Moreover, a large structural disorder of the Cu local environment is evident, consistent with the above-mentioned high mobility of Cu^{I} ions, even if coordinated to the zeolite framework.

To get further insights in the Cu-species present in the catalysts during e1-e3, we examined the time evolution of the XANES spectra, both as a function of time at 100 °C after NH_3 adsorption (Figure 3a,c,e), and as a function of temperature/time during TPD/TPSR (Figure 3b,d,f).

In the first step at 100 °C, time-resolved XANES indicated a quick mobilization by NH_3 of the Cu-ions in the catalyst. Already after ~10 min from NH_3 dosage, the characteristic XAS features of framework-coordinated Cu^{II} and Cu^{I} ions have disappeared, replaced by the spectral signatures of Cu-amino complexes.

Linear Cu^{I} species, fingerprinted by the XANES peak at 8983 eV, are initially more abundant if the material is activated in *vacuum* (e2, Figure 3c). In this case, the subsequent intensity development of the 8983 eV peak as a function of time from NH_3 adsorption is limited. In the other two experiments - e1 and e3 - the catalyst prior to NH_3 dosage only contains a minor amount of ZCu^{I} species, while most of the Cu is in the +2 oxidation state. While the initial intensity of the 8983 eV peak after NH_3 adsorption is lower than in e2, it progressively increases with time, at a much faster rate under a 1% NO/He gas flow (e3).

In all the experiments, the temperature increase initially resulted in the further development of the XANES features of linear Cu^{I} at the expenses of NH_3-ligated Cu^{II} moieties. However, as can be observed in Figure 3b,d,f, the evolution of the 8983 eV peak is not monotonous: after ca. 450 °C its intensity starts to decrease. Simultaneously, the broad peak at 8989 eV develops, pointing to further transformations involving the NH_3-derived Cu^{I} complexes.

In the following section, we will elaborate the qualitative insights reported so far into a quantitative evaluation of Cu-speciation during e1-e3, by applying XANES LCF and MCR analysis to the time-dependent dataset in Figure 3.

3.2 Evaluation of Cu-speciation by XANES LCF and MCR analysis

3.2.1 Cu-speciation in the activated catalyst. Prior to examining the *in situ* data collected after interaction with NH_3, a first step in our analysis was to evaluate the Cu-speciation in the O_2- and *vacuum*-activated material. As detailed in Section 2.2.4, to this aim we used as references the MCR-derived spectra of the five Cu-species illustrated in Figure 4a, obtained in a previous study.[9]

Figure 4b,c reports the percentages of Cu-species found after O_2- and *vacuum*-activation at 400 °C. The high quality of the LCF can be appreciated in Figure 4d,e, comparing experimental and best fit XANES spectra for the O_2- and *vacuum*-activated catalyst, resulting in R-factors as low as 1.1×10^{-4} and 2.7×10^{-4}, respectively.

The O_2-activated state mostly contains $Z[Cu^{II}(OH)]$ species, and similar species with the same tridentate coordination geometry as $Z[Cu^{II}(OH)]$ (Figure 4, grey box), such as mono-copper(II) superoxides $Z[Cu^{II}OO^{\bullet}]$ [9-11]. A small fraction of ZCu^{I} (17% total Cu) is found, which gives rise to the weak shoulder at 8983 eV in the XANES (see Figure 4d). About 9% of the Cu is present in under-coordinated Cu^{II} aquo-complexes. Z_2Cu^{II} species are not detected within the sensitivity of the method (ca. 5% total Cu).

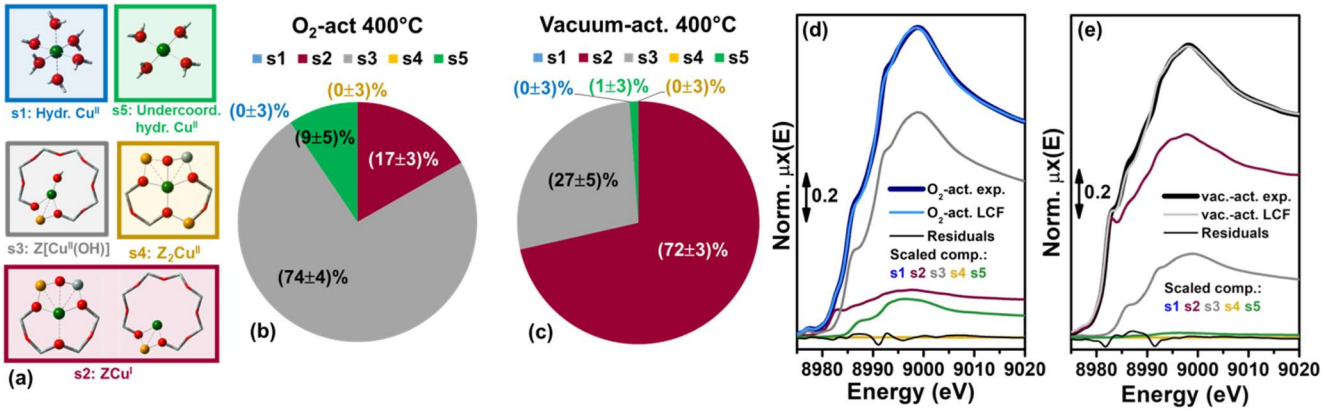

Figure 4. (a) Molecular models of the five pure Cu-species considered in the LCF model; atom colour code: Cu, green; H, white; O, red, Si, grey, Al, yellow. (b, c) Pie charts illustrating Cu-speciation in (b) the O_2-activated and (c) the *vacuum*-activated catalyst at 400 °C, as estimated by XANES LCF analysis using as references the five pure spectra obtained by MCR analysis in ref.[9] for the Cu-species shown in part (a), using the same colour code; statistical LCF errors on the percentage of Cu-species are also indicated. (d, e) Comparison between experimental and best-fit spectra for (d) O_2- and (e) *vacuum*-activated Cu-CHA. The LCF residuals and the five scaled components are also reported.

Activation in *vacuum* leads to the formation of a substantial fraction of ZCu^I species (72% total Cu), indicating 'self-reduction' of redox-active $Z[Cu^{II}(OH)]$ moieties.[6, 8, 9, 45, 46, 64, 65] Nonetheless, at the experimental conditions adopted, we also observe 27% of Cu still in the form of $Z[Cu^{II}(OH)]$ after 60 min in *vacuum* at 400 °C. Consistently with the LCF results for the O_2-activated material, the fraction of Z_2Cu^{II} ions in 6MR fall below the method detection limit also after *vacuum*-activation. The XANES spectra collected on the activated catalyst cooled to 100 °C just prior to NH_3 dosage shows only minor modifications (see Figure 3a,c). Thus, the Cu-speciation evaluated at 400 °C represents, under a reasonable approximation, the state of the Cu in the material before interaction with NH_3 at 100 °C.

3.2.2 Nature of NH_3-derived Cu-species. To extract quantitative information on Cu-speciation in the catalyst during interaction with NH_3 and TPD/TPSR, we have applied the MCR method to the *in situ* XAS dataset reported in Figure 3. Previous studies have shown that XANES LCF based on measured spectra of the $[Cu^{II}(NH_3)_4]^{2+}$ and the $[Cu^{I}(NH_3)_2]^{+}$ complexes (see Figure 2a) provides good estimates for the Cu oxidation state in the presence of NH_3, NH_3+NO, or an SCR reaction feed below 200 °C. [3, 7, 8, 13, 14, 16, 23, 49, 66] However, as explained above, further structural and chemical transformations occur at higher temperatures, which cannot be described based on the solution-phase-like Cu^I- and Cu^{II}-amino complexes alone. Thus, we adopted the state-of-the-art MCR approach (see Section 2.2.5 for details) to assess the number and the nature of Cu-species present in the investigated Cu-CHA catalyst under the e1-e3 experimental conditions.

Figure 5 reports an overview of the MCR-results, in terms of 'pure' XANES spectra (Figure 5a) and concentration profiles (Figure 5c-e for e1-e3, respectively) of the four Cu-species identified by PCA. Considering the characteristic XANES features of the MCR spectra together with their correspondent time/temperature dependent dynamics, we connected the identified PCs with the four Cu-species illustrated in Figure 5b. We assign PC1 to a Cu^{II} species, exhibiting a XANES spectrum very similar to the one of $[Cu^{II}(NH_3)_4]^{2+}$. The weak peak in the Cu^I 1s→4p energy range observed in the PC1 MCR spectrum (blue asterisk in Figure 5a) is most likely an artefact of the reconstruction. Indeed, the absence of a time window where exclusively Cu^{II} species are present and the remarkable intensity of the Cu^I peak in PC3 and PC4, could cause a trace of this feature to be fictitiously embedded also in the PC1 MCR curve.

Notably, the XANES features correspond to the ones observed for $[Cu^{II}(NH_3)_4]^{2+}$, characteristic of NH_3-ligated Cu^{II} centers,[67] but they are significantly broadened with respect to the solution-phase complex, the double component in the white-line peak being much less pronounced. In line with the strongly coordinating nature of NH_3 and previous valence-to-core X-ray emission spectroscopy (vtc-XES) results under low-temperature SCR conditions,[23] all these

evidences are consistent with NH_3-solvated mixed-ligand Cu^{II} species, structurally similar to $[Cu^{II}(NH_3)_4]^{2+}$ but having one of the four first-shell NH_3 ligands replaced by an O-containing moiety. Considering the Cu^{II} species present in the catalyst prior to NH_3 dosage (see Section 3.2.1), the possibilities consistent with XAS results are reported here below:

$$Z[Cu^{II}(OH)] + 3\ NH_3 \rightarrow Z\cdots[Cu^{II}(NH_3)_3(OH)] \quad (1)$$

$$Z[Cu^{II}(OO^{\bullet})] + 3\ NH_3 \rightarrow Z\cdots[Cu^{II}(NH_3)_3(OO^{\bullet})] \quad (2)$$

$$Z_2Cu^{II} + 4\ NH_3 \rightarrow Z_2\cdots[Cu^{II}(NH_3)_4] \quad (3)$$

where the symbol ··· refers to mobile Cu-complexes electrostatically tethered to a Z or Z_2 exchange site of the zeolite, but without a chemical bond with the zeolitic framework.

We expect a very minor contribution from Z_2 ··· $[Cu^{II}(NH_3)_4]$, because no significant contribution of Z_2Cu^{II} sites was detected in this specific Cu-CHA sample (Cu/Al = 0.444 and Si/Al = 13.1) after activation (see Section 3.2.1). Also, all the Cu-species formed in eqs. (1)-(3) are expected to show very similar XANES spectra, so that they can plausibly lump into a single PC: in all cases we are dealing with (pseudo-) square-planar-like Cu^{II} complexes. PC1 is consequently connected with $[Cu^{II}(NH_3)_3(X)]^{n+}$ species, where X = NH_3 (n = 2), OH or $OO^{\bullet}$ (n = 1). Notably, $[Cu^{II}(NH_3)_3(OH)]^{+}$ complexes have been envisaged as relevant species in recently proposed mechanisms for low-temperature NH_3-SCR.[8]

All the other PCs correspond to Cu^{I} species. Analysing the concentrations profiles in Figure 5c-e, is it clear that, upon increasing the temperature, the three Cu^{I} species form in the sequence PC3 → PC4 →PC2. The MCR spectrum of PC3 is in excellent agreement with the one of the $[Cu^{I}(NH_3)_2]^{+}$ model compound measured in the solution phase (Figure 5a, wine dashed curve). Thus, we assign PC3 to solution-phase like $[Cu^{I}(NH_3)_2]^{+}$. Such species could be firstly formed through NH_3 solvation of ZCu^{I} species already present in the catalyst due to self-reduction during activation:

$$ZCu^{I} + 2\ NH_3 \rightarrow Z\cdots[Cu^{I}(NH_3)_2] \quad (4)$$

PC4 shows a XANES spectrum similar the one assigned to the $[Cu^{I}(NH_3)_2]^{+}$ species. The sharp and intense peak at 8983 eV is diagnostic, also in this case, for a linear Cu^{I} species. However, the PC4 MCR curve differs in the white-line region, and shows a higher normalized absorption in the 8985-8992 eV range with respect to PC3 one. $Z[Cu^{I}(NH_3)]$, formed by desorption of one NH_3 ligand from mobile $[Cu^{I}(NH_3)_2]^{+}$ complexes, has been investigated by theory in a number of reports.[15, 27, 35, 68] DFT models in 6MR predict a linear Cu^{I} complex coordinated to one framework O atom in the proximity of the charge-balancing Al site and to the residual NH_3 molecule, where Cu is significantly lifted from the zeolite ring plane. This geometry is in good agreement with the characteristic of the PC4 MCR spectrum, supporting its assignment to a $Z[Cu^{I}(NH_3)]$ species.

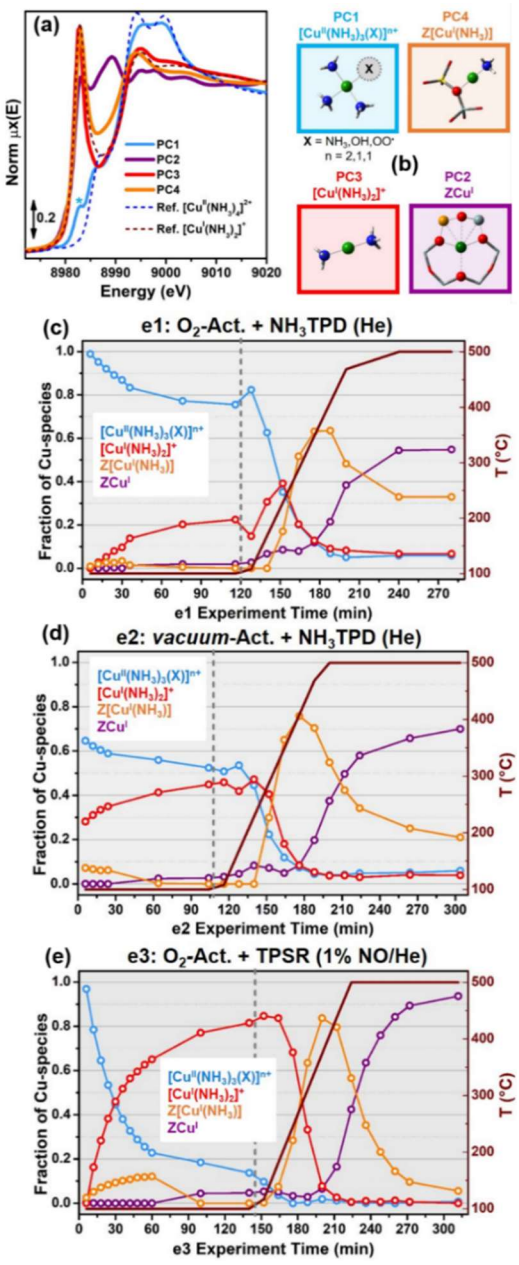

Figure 5. (a) 'Pure' XANES spectra obtained from MCR analysis of the *in situ* XAS dataset collected during e1-e3 (experimental spectra reported in Figure 3). The reference spectra of the $[Cu^{II}(NH_3)_4]^{2+}$ (blue dashed line) and $[Cu^{I}(NH_3)_2]^{+}$ (wine dashed line) complexes (measured at RT in the solution phase) are reported for comparison. (b) Illustration of the Cu-species assigned to the 4 PCs identified in the dataset, using the same colour code as in part (a) for the corresponding pure spectra. (c-e) Concentration profiles of the four Cu-species corresponding to the pure XANES spectra in part (a) during experiments (c) e1, (d) e2 and (e) e3. For all the experiments, the temperature profile is reported as a dark red line, and corresponding values are given on the right ordinate axis. The vertical grey dashed lines demark the beginning of the heating ramp from 100 to 500 °C for the TPD/TPSR step of the experiments.

Finally, PC2, develops in all the experiments from T > 300 °C concomitantly to the decay in the population of $Z[Cu^{I}(NH_3)]$ (PC4). Its theoretical spectrum shows several resonances at energy positions comparable with what is observed after *vacuum*-activation at 400 °C. The relative intensity of the XANES features is however different, with a general enhancement of the rising-edge features to the expenses of the white-line intensity. Notably, the PC2 MCR spectrum is in excellent agreement with the one obtained from MCR-analysis of HERFD-XANES spectra collected on a Cu-CHA material with similar composition as used here (Si/Al = 12, Cu/Al = 0.5) upon activation in He at 500 °C.[11] It is thus plausible to assign PC2 to ZCu^{I} sites, formed upon complete desorption/consumption of

NH_3 ligands. The differences in the ZCu^I XANES signature after *vacuum*-activation at 400 °C and after TPD/TPSR at 500 °C suggest a preferential population of one amongst the two sites – in 8MR and 6MR (see Figure 4a, red box) - previously proposed for Cu^I ions in the CHA framework.[6, 9, 12] The higher intensity of the XANES rising edge peak points to a more linear Cu^I coordination geometry, and could thus indicate ZCu^I to preferentially stabilize in 6MR rather than 8MR (O–Cu–O bond angles of 142° and 82° in 6MR and 8MR, respectively, according to DFT models in ref.[6]). This assignment would also be in agreement with the computed energetics of ZCu^I in the 6MR vs the 8MR.[7, 68] In this respect, we have performed preliminary EXAFS fits on the spectrum collected at 500 °C at the end of e3 (Figure 2d, purple curve), containing ca. 95% of PC2 according to MCR results in Figure 5e. EXAFS analysis indicated a first-shell of O_{fw} atoms with coordination number $N_{Ofw} = 1.6 \pm 0.4$ and average bond distance $\langle R_{O(fw)} \rangle = (1.93 \pm 0.02)$ Å, consistent with the DFT-optimized model of ZCu^I in the 6MR ($N_{Ofw}^{DFT} = 2$; $\langle R_{O(fw)} \rangle^{DFT} = 1.96$ Å, Figure 5b, purple box). Unfortunately, it was impossible to obtain conclusive results on the subsequent coordination shells, due to the limited EXAFS data quality and the high level of thermal and structural disorder present under these conditions. Future experiments aiming at improved quality in the high k-space range would be decisive to get more accurate and reliable fitting results.

3.2.3 Dynamics and thermal stability of NH_3-derived Cu-species. Having identified the chemical nature of the four structural components in e1-e3, we can now analyse their dynamics in the view of the characteristic conditions adopted in the three experiments. Let us first consider e1 and e2 (Figure 5c,d), which provide us direct information on the thermal stability of NH_3-derived Cu-species in the catalyst.

During the isothermal step at 100 °C, the Cu-speciation is dominated by a mixture of $[Cu^{II}(NH_3)_3(X)]^{n+}$ (PC1) and $[Cu^{I}(NH_3)_2]^+$ (PC3). The initial Cu^{II}/Cu^I ratio correlates with Cu-speciation in the activated material. *Vacuum*-activation in e2 yields to 30% of Cu^I already at the beginning of the NH_3-experiment (t = 0 in Figure 5d), while after O_2-activation (t = 0 in Figure 5c) virtually all the Cu is found as $[Cu^{II}(NH_3)_3(X)]^{n+}$ species (PC1). In both the experiments a progressive PC1 to PC3 conversion is observed as a function of time at 100 °C. After ca. 2 h in He at 100 °C, the Cu^I fraction reaches 24% and 48% total Cu in e1 and e2, respectively. We note that due to the small Cu^I 'contamination' in the MCR spectrum of PC1, the fraction of Cu^I is expected to be underestimated by ca. 10% total Cu. Moreover, during NH_3 dosage at 100 °C, $[Cu^{I}(NH_3)_4]^+$ complexes could be also formed. Computational studies indicate that these four-fold coordinated Cu^I species would be very prone to desorb two NH_3 ligands and transform to linear $[Cu^{I}(NH_3)_2]^+$ once NH_3 is removed from the cell.[15] The $[Cu^{I}(NH_3)_4]^+$ XANES spectrum is expected to be much closer to the one of PC1 (a four-fold coordinated Cu^{II} species) rather than to the one of PC3 (a linear Cu^I species), due to the different splitting of Cu 4p orbitals in Cu^I sites with different coordination numbers.[69, 70] Thus, during the isothermal step at 100 °C, these species could be also spuriosuly included in the PC1 component, also causing an underestimation of the global Cu^I fraction in the catalyst. Moreover, minor (< 10 total Cu %, based on the similarity of the XANES, see Figure 3c) re-oxidation of ZCu^I to $Z[Cu^{II}(OH)]$ in the *vacuum*-activated catalyst cannot be excluded while cooling from 400 to 100 °C prior to NH_3 dosage in e2, due to traces of moisture soaking into the reactor cell.

Taken together, these factors can account for the lower amount of Cu^I found at 100 °C in e2 (48%) with respect to the *vacuum*-activated material (72% total Cu, see Section 3.2.1). Despite such possible causes for Cu^I underestimation, in e1 the fraction of Cu^I after interaction with NH_3 and stabilization at 100 °C in He flow (24%) is higher than in the O_2-activated material (17%). This result points to redox pathways involving $[Cu^{II}(NH_3)_3(X)]^{n+}$ species, concomitant of NH_3 desorption phenomena, in action to a minor extent already at 100 °C and favoured at higher temperature. Indeed, from the very beginning of the heating ramp from 100 to 500 °C, a steep decrease in the PC1 contribution in the favour of Cu^I species is observed for both e1 and e2 (NH_3-TPD in He). The PC1 fractions level off at values < 10% total Cu around 400 °C in both cases. The calculations by Chen et al.,[27] predicted a significantly lower NH_3 desorption energy for $[Cu^{II}(NH_3)_3(OH)]^+$ with respect to pure Cu^{II}-tetramine species hosted in the CHA framework. NH_3 desorption from the first mixed-ligand complex is foreseen to contribute to the two NH_3-TPD peaks experimentally observed below 200 °C and in the 250-350 °C range.[28-30] Conversely, NH_3 desorption from $[Cu^{II}(NH_3)_4]^{2+}$ is associated with the higher temperature peak appearing in the

400-500 °C range in NH_3-TPD experiments. These evidences reinforce our assignment of PC1 to a large majority of mixed-ligand Cu^{II} moieties such as $[Cu^{II}(NH_3)_3(OH)]^+$, efficiently desorbing NH_3 before 350 °C.

Driven by the relevance of mobile $[Cu^{I}(NH_3)_2]^+$ complexes in the low-temperature NH_3-SCR mechanism,[14, 15, 71] we examined in more detail the temperature-dependent evolution of $[Cu^{I}(NH_3)_2]^+$ and $Z[Cu^{I}(NH_3)]$. As summarized in Table 2, the $[Cu^{I}(NH_3)_2]^+$ concentration reach its maximum at 230 °C (hereafter, T_c^{MAX}) in both e1 and e2. Afterwards, it decreases with temperature, arriving at concentration lower that 10% total Cu at 410 °C (hereafter, $T_c^{<10\%}$). These values are in very good agreement with the theoretical NH_3 desorption peak from $[Cu^{I}(NH_3)_2]^+$ in Cu-CHA simulated from first principles by Chen et al., approximately ranging from 200 to 400 °C with maximum desorption at ca. 350 °C (see also last column in Table 2).

T_c^{MAX} for the $Z[Cu^{I}(NH_3)]$ species is also found at ca. 410 °C, matching the $T_c^{<10\%}$ for $[Cu^{I}(NH_3)_2]^+$ as expected in the case of a progressive transformation of the latter species into the first. $Z[Cu^{I}(NH_3)]$ undergoes a slower decay with temperature, converting into NH_3-free ZCu^{I} species (PC2): at the end of both e1 and e2 (500 °C in He) its concentration levels off to 25-30 % total Cu. Also this results is consisted with the theoretical study cited above, which indicates desorption from $Z[Cu^{I}(NH_3)]$ until ca. 550 °C, a temperature which is not reached in our experiments. Notice that certain differences in the T_c^{MAX} estimated in this work and literature works could be related to the employed experimental set-up, using pelletized samples in a reactor cell characterized by a large dead volume and a not-passing-through gas flow.

The Cu-speciation in e3, carried out in a 1% NO/He flow, follows the same trends outlined above. However, in line with a number of previous studies,[8, 13, 63] the compresence of NH_3 (in this case pre-adsorbed at Lewis and Brønsted acid sites in the catalyst) and gas-phase NO greatly favours the Cu^{II} to Cu^{I} reduction. Under the conditions of e3, ca. 80% of Cu is found as $[Cu^{I}(NH_3)_2]^+$ already at 100 °C. The presence of NO during the heating step also speed up the $Z\cdots[Cu^{I}(NH_3)_2]^+ \rightarrow Z[Cu^{I}(NH_3)] \rightarrow ZCu^{I}$ cascade conversion: both T_c^{MAX} and $T_c^{<10\%}$ for NH_3-derived Cu^{I} species lower significantly with respect to the values observed in e1 and e2 (Table 2).

Table 2. Key temperatures in the MCR concentration profiles of $[Cu^{I}(NH_3)_2]^+$ (PC3) and $Z[Cu^{I}NH_3]$ (PC4) (T_c^{MAX}: temperature corresponding to the maximum concentration detected; $T_c^{<10\%}$: first temperature when a concentration < 10% total Cu is detected) during experiments e1, e2 and e3. The temperature ranges for the NH_3 desorption peaks simulated by Chen et al.[27] are reported for comparison in the last column.

Cu-species	e1 *vac.-act., NH_3-TPD*		e2 *vac.-act., NH_3-TPD*		e3 *O_2-act., NH_3-NO-TPSR*		T_{des}^{start}–T_{des}^{end} [T_{des}^{MAX}]^a
	T_c^{MAX}	$T_c^{<10\%}$	T_c^{MAX}	$T_c^{<10\%}$	T_c^{MAX}	$T_c^{<10\%}$	
	(°C)		(°C)		(°C)		(°C)
$[Cu^{I}(NH_3)_2]^+$	230	410	230	410	120	370	200–400 [350]
$Z[Cu^{I}NH_3]$	410	n.d.	410	n.d.	370	500	300–550 [460]

In summary, results from e1 demonstrate that NH_3 alone is capable to reduce Cu, but much less efficiently with respect the NH_3 + NO mixture (e3). Starting from the lowest temperature probed in this work, 100 °C, NH_3 first acts as a solvating ligand for the Cu ions, initially preserving their pristine activation-dependent oxidation state. Thus, a larger initial fraction of Cu^{I} directly yields to a larger population of $[Cu(NH_3)_2]^+$ in fixed time/temperature frame. Conversely, NH_3 solvation of Cu^{II} ions will firstly yield $[Cu^{II}(NH_3)_3(X)]^{n+}$ species, needing a further reduction step to form $[Cu(NH_3)_2]^+$. Consequently, the overall conversion cascade during NH_3-TPD proceeds more efficiently in the former case, providing a rational from the higher fraction of bare ZCu^{I} found in the final state of e2 (from *vacuum*-activation) with respect to e1 (O_2-activation).

3.3 Complementary insights from in situ DR UV-Vis-NIR spectroscopy

DR UV-Vis-NIR spectroscopy was used as complementary technique to follow the reactivity of Cu^{II} ions with NH_3. In particular, we were interested in providing additional evidences about the reducing ability of NH_3 towards Cu^{II} ions obtained after O_2-activation, similarly to what observed in experiment e1. The assignment of the UV-Vis features in heterogeneous catalysts is usually not straightforward, even in structurally well-defined systems such as

Cu-zeolites.[7, 72] Both ligand field *d*–*d* transitions and charge transfer (CT) can be strongly affected in both intensity and frequency by the nature of ligands and local symmetry of the metal ions. This implies that the spectroscopic fingerprint of Cu-CHA (the well-known quadruplet)[34] could be related to one of the proposed Cu^{II} sites ($Z[Cu^{II}(OH)]$, Z_2Cu^{II} or $Z[Cu^{II}(OO^{\bullet})]$) or, more likely results from an overlap of bands originating from the three different structures. Moreover, we cannot exclude a contribution from Cu^{II} ions involved in multimeric Cu-oxo complexes.[7, 34, 73, 74] Notwithstanding this complexity, interesting pieces of information can be obtained by *in situ* measurements following the evolution of Cu^{II} electronic transitions during the interaction with NH_3. On the other hand, the structures extracted with the MCR approach could be used for a more precise assignment of the observed features.

Figure 6 reports the spectra obtained during the isothermal exposure of the O_2-activated catalyst to 1200 ppm of NH_3 at 200 °C (Figure 6a) and during subsequent heating in the same gas feed (Figure 6b). The spectra are here plotted as R%, to avoid the possible artefacts connected to the use of the Kubelka-Munk function.[75, 76] Ammonia was dosed on the O_2-activated catalyst (previously activated at 400 and cooled in O_2 at 200 °C), whose peculiar spectrum is reported as a dotted line in Figure 6a. The spectrum of the sample is dominated by a broad band with a quadruplet shape in the *d*–*d* transition region, which is well documented in the literature for O_2-activated Cu-CHA.[34, 36, 73, 77, 78] Furthermore, a well-defined shoulder around 32000 cm^{-1} is present in the low energy tail of the CT transition. An unambiguous attribution of this spectral component to a structurally defined Cu species is still an ongoing challenge. Indeed, different copper-oxo complexes – both monomeric and multimeric - might give rise to signals in this region.[7, 34, 73, 74]

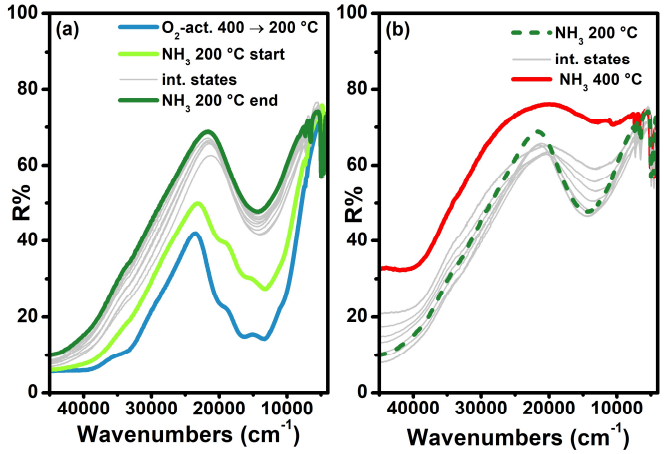

Figure 6. *In situ* DR UV-Vis-NIR spectra of the Cu-CHA catalyst during exposure to 1200 ppm NH_3 at 200 °C for 120 min, after activation in O_2 at 400°C and cooling in O_2 at 200 °C. (b) *In situ* DR UV-Vis-NIR spectra of the Cu-CHA catalyst during heating to 400 °C in NH_3. Spectra plotted in R%.

Upon exposure to NH_3, we do observe changes in the entire spectral region. In the NIR region, the overtones and combination modes associated with the presence of adsorbed NH_3 and NH_4^+ species grow with exposure time. The intensity of the quadruplet *d*–*d* feature is affected immediately, together with the 32000 cm^{-1} shoulder. While prolonging NH_3 exposure, these features are transformed into a new one, which is still ascribable to Cu^{II} ions, due to the presence of a band with *d*–*d* character centred at 14100 cm^{-1}. Based on LCF analysis with measured $[Cu^{II}(NH_3)_4]^{2+}$ and $[Cu^{I}(NH_3)_2]^{+}$ references, NH_3 dosage at 200 °C on O_2-activated Cu-CHA has been reported to result in a mixture of Cu^{II} and Cu^{I} amino-complexes (roughly 75% and 25%, respectively).[13] Since closed-shell Cu^{I} ions cannot be involved in *d*–*d* transitions, the observed *d*–*d* band at 14100 cm^{-1} and CT transition at 31200 cm^{-1} (measured at half height) are ascribable to the $[Cu^{II}(NH_3)_3(X)]^{n+}$ complexes predicted on the basis of the XAS analysis described above. Indeed, in aqueous solution $[Cu^{II}(NH_3)_4]^{2+}$ complexes are reported to absorb around 17000 cm^{-1}, while lower frequencies are found for $[Cu^{II}(NH_3)_n]^{2+}$ with n<4, due to the insertion of H_2O/OH^- ligands in the coordination sphere of the metal ion.[79] The mobilization of Cu^{II} ions, passing from framework O atoms to NH_3 ligands, is also testified by the blue-shift of the CT transition. This is in fact expected to move to higher

frequency by decreasing the optical electronegativity of the ligands.[80, 81] The presence of water in the coordination sphere of Cu^{II} ions can be safely discarded due to the absence of the overtone and combination modes of physisorbed water in the NIR region (not reported).

The observed decrease in intensity in Figure 6a cannot be used for a quantitative estimation of the amount of reduced copper. Indeed, a change in the metal ion symmetry (passing from framework interacting ions to more symmetrical NH_3-solvated ones) is expected to decrease the corresponding extinction coefficient. Conversely, in agreement with XAS results, the spectra reported in Figure 6b provide evident indications of the concentration rise of Cu^{I} species during the heating ramp to 400 °C, as indicated by the disappearance of bands in the *d-d* region. The reduction proceeds gradually with the temperature increase, with major changes above 300 °C. The final state reached at 400°C is that of a fully reduced catalyst (the peak at 10000 cm^{-1} is an artefact due to bad background compensation), possibly with a mixture of $[Cu^{I}(NH_3)_2]^+$/ $Z[Cu^{I}(NH_3)]$ species. We cannot exclude a contribution also from 'bare' ZCu^{I} sites.

This hypothesis is also confirmed by the blue-shift of the CT transitions (from 31200 to 35500 cm^{-1}), which is in agreement with the expected change passing from divalent to monovalent metal centres.[80-82] Moreover, the spectrum measured *ex situ* at RT after exposure to NH_3 at 400 °C (not reported) show CT band at higher frequency (39500 cm^{-1}). We can hypothesize that in these conditions $[Cu^{I}(NH_3)_2]^+$ complexes are the main species, while at 400 °C a consistent fraction of framework interacting $Z[Cu^{I}(NH_3)]$ sites is responsible for the observed red-shift.

These results nicely fit with the detailed XAS analysis described above. First, they confirm the occurrence of redox phenomena in a NH_3-only feed, favoured as temperature increases from 200 to 400 °C. Secondly, the observed positions of the *d-d* and CT absorption (also in comparison with reference data)[79] are in good agreement with the presence of mixed-ligand Cu^{II} and Cu^{I} amino moieties.

4. Conclusions

In this work we explored by *in situ* XAS and UV-Vis-NIR spectroscopy the nature and thermal stability of NH_3-derived Cu^{I} and Cu^{II} species in an industrially-relevant Cu-CHA deNO_x catalyst. Both the techniques confirm a fast and complete 'solvation' by NH_3 of the framework-coordinated Cu ions formed upon thermal activation of the catalyst. Interaction with NH_3 in the 100-200 °C range drives the Cu in the material in a quasi-mobile state (Cu^{I} and Cu^{II}-amino complexes fully detached from the framework, but electrostatically tethered to charge-balancing exchange sites in the zeolite). All our spectroscopic evidences indicate that NH_3 desorption at T > 200 °C is accompanied by $Cu^{II} \rightarrow Cu^{I}$ reduction phenomena, also in the absence of NO. In line with previous reports, the simultaneous presence of NH_3 (pre-adsorbed and/or in the gas phase) and gas-phase NO largely enhances and speeds up the reduction effect. Notice that this is at variance with respect to XAS/XES observations in the presence of the whole SCR mixture, pointing to the formation of a dominant fraction of framework interacting Cu^{II} ions above 250 °C.[23] These insights corroborate some of the most innovative concepts developed in the last years in the field of NH_3-SCR over Cu-zeolite catalysts, that are the impact of reaction conditions on the nature of the Cu-species present, as well as the relevance of $Z\cdots[Cu^{I}(NH_3)_2]$ species in the low-temperature reaction mechanism.[7]

Aiming to achieve a deeper understanding of the NH_3-derived Cu-species formed in Cu-CHA, in this work we have applied MCR analysis to extract quantitative information from *in situ* XANES data. Despite some inherent limitations of the method, this statistical/chemometric approach allowed us to access a much higher level of detail with respect to LCF analysis using experimental spectra of $[Cu^{I}(NH_3)_2]^+$ and $[Cu^{II}(NH_3)_4]^{2+}$ model compounds. The MCR results, providing 'pure' spectra and concentration profiles of the Cu-species present during *in situ* XAS experiments, are interpreted in comparison to experimental and theoretical reports focusing on NH_3-TPD profiles for Cu-CHA.[27-30]

The most relevant points emerging from MCR analysis include: (i) formation of mixed-ligand amino-Cu^{II} moieties such as $Z\cdots[Cu^{II}(NH_3)_3(OH)]$, undergoing NH_3 desorption from temperatures as low as 100 °C; (ii) experimental validation of the temperature range for NH_3 desorption from $Z\cdots[Cu^{I}(NH_3)_2]$, identified here as 230-410 °C, in agreement with the computational prediction by Chen et al.[27]; (iii) deconvolution of the contributions from quasi-

mobile Z···[$Cu^{I}(NH_3)_2$] and framework-coordinated Z[$Cu^{I}(NH_3)$] and isolation of the XANES spectrum of the latter species; (iv) structural sensitivity to the final NH_3 desorption step Z[$Cu^{I}(NH_3)$] → ZCu^{I} + NH_3 and possible preferences for 6MR sites.

Notably, the possibility to discriminate by XANES the structurally similar Z···[$Cu^{I}(NH_3)_2$] and Z[$Cu^{I}(NH_3)$] species is crucial to accurately determine by XAS the transition from quasi-mobile species - capable of O_2-activation by transient pair formation[14, 15, 71] - to 'immobile' Z[$Cu^{I}(NH_3)$] species with O_{fw}-Cu^{I}-NH_3 ligation. As also observed by Chen et al.[27] based on simulated NH_3-TPD profiles, the concentration rise of Z[$Cu^{I}(NH_3)$] well corresponds to the dip in NO conversion often observed in the 300-350 °C range for NH_3-SCR over Cu-CHA catalysts. O_2-activation over this intermediate, demarking the transition from low- and high-temperature SCR regimes, is indeed likely hampered with respect to 'bare' ZCu^{I}, due to the residual NH_3-ligand.

Overall, the information obtained here expands the fundamental knowledge basis required to unravel the NH_3-SCR mechanism over Cu-CHA, across the whole temperature range of interest for industrial applications. Future studies in this direction could exploit the pure MCR spectra obtained here and further validate our assignments by DFT-assisted XANES simulations of the proposed Cu-species.

Conflicts of interest

There are no conflicts to declare.

Acknowledgements

CL acknowledges the Mega-grant of the Russian Federation Government to support scientific research at the Southern Federal University, No. 14.Y26.31.0001. We are grateful to Filippo Giordanino for his contribution in designing and performing the XAS experiments and to Haldor Topsøe A/S for financial support to his Ph.D. project. We also thank Andrea Lazzarini for support during the XAS data collection, Andrea Martini for programming the script for XANES LCF and for advices on MCR analysis, Pablo Beato for insightful discussions and support in the interpretation of the results, Olivier Mathon for his competent assistance during the XAS measurements on the BM23 beamline of the ESRF. We are grateful to Silvia Bordiga for insightful advices and constant scientific support.

Notes and references

1. *Air quality in Europe - 2018 report, EEA Report No 12/2018*, 2018.
2. *EU Clean Vehicles Directive*, downloadable at https://ec.europa.eu/transport/themes/urban/vehicles/directive_en.
3. A. M. Beale, F. Gao, I. Lezcano-Gonzalez, C. H. F. Peden and J. Szanyi, *Chem. Soc. Rev.*, 2015, **44**, 7371-7405.
4. J. H. Kwak, R. G. Tonkyn, D. H. Kim, J. Szanyi and C. H. F. Peden, *J. Catal.*, 2010, **275**, 187-190.
5. S. J. Schmieg, S. H. Oh, C. H. Kim, D. B. Brown, J. H. Lee, C. H. F. Peden and D. H. Kim, *Catal. Today*, 2011, **184**, 252-261.
6. E. Borfecchia, K. A. Lomachenko, F. Giordanino, H. Falsig, P. Beato, A. V. Soldatov, S. Bordiga and C. Lamberti, *Chem. Sci.*, 2015, **6**, 548-563.
7. E. Borfecchia, P. Beato, S. Svelle, U. Olsbye, C. Lamberti and S. Bordiga, *Chem. Soc. Rev.*, 2018, **47**, 8097-8133.
8. C. Paolucci, A. A. Parekh, I. Khurana, J. R. Di Iorio, H. Li, J. D. Albarracin Caballero, A. J. Shih, T. Anggara, W. N. Delgass, J. T. Miller, F. H. Ribeiro, R. Gounder and W. F. Schneider, *J. Am. Chem. Soc.*, 2016, **138**, 6028-6048.
9. A. Martini, E. Borfecchia, K. A. Lomachenko, I. A. Pankin, C. Negri, G. Berlier, P. Beato, H. Falsig, S. Bordiga and C. Lamberti, *Chem. Sci.*, 2017, **8**, 6836-6851.
10. D. K. Pappas, E. Borfecchia, M. Dyballa, I. A. Pankin, K. A. Lomachenko, A. Martini, M. Signorile, S. Teketel, B. Arstad, G. Berlier, C. Lamberti, S. Bordiga, U. Olsbye, K. P. Lillerud, S. Svelle and P. Beato, *J. Am. Chem. Soc.*, 2017, **139**, 14961-14975.
11. A. Martini, E. Alladio and E. Borfecchia, *Top. Catal.*, 2018, **61**, 1396-1407.
12. C. W. Andersen, E. Borfecchia, M. Bremholm, M. R. V. Jorgensen, P. N. R. Vennestrom, C. Lamberti, L. F. Lundegaard and B. B. Iversen, *Angew. Chem.-Int. Edit.*, 2017, **56**, 10367-10372.

13. T. V. W. Janssens, H. Falsig, L. F. Lundegaard, P. N. R. Vennestrøm, S. B. Rasmussen, P. G. Moses, F. Giordanino, E. Borfecchia, K. A. Lomachenko, C. Lamberti, S. Bordiga, A. Godiksen, S. Mossin and P. Beato, *ACS Catal.*, 2015, **5**, 2832-2845.
14. C. Paolucci, I. Khurana, A. A. Parekh, S. C. Li, A. J. Shih, H. Li, J. R. Di Iorio, J. D. Albarracin-Caballero, A. Yezerets, J. T. Miller, W. N. Delgass, F. H. Ribeiro, W. F. Schneider and R. Gounder, *Science*, 2017, **357**, 898-903.
15. L. Chen, H. Falsig, T. V. W. Janssens and H. Gronbeck, *J. Catal.*, 2018, **358**, 179-186.
16. A. Marberger, A. W. Petrov, P. Steiger, M. Elsener, O. Krocher, M. Nachtegaal and D. Ferri, *Nat. Catal.*, 2018, **1**, 221-227.
17. C. Tyrsted, E. Borfecchia, G. Berlier, K. A. Lomachenko, C. Lamberti, S. Bordiga, P. N. R. Vennestrom, T. V. W. Janssens, H. Falsig, P. Beato and A. Puig-Molina, *Catal. Sci. Technol.*, 2016, **6**, 8314-8324.
18. C. Negri, P. S. Hammershøi, T. V. W. Janssens, P. Beato, G. Berlier and S. Bordiga, *Chem. Eur. J.*, 2018, **24**, 12044-12053.
19. M. P. Ruggeri, I. Nova, E. Tronconi, J. A. Pihl, T. J. Toops and W. P. Partridge, *Appl. Catal. B: Environ.*, 2015, **166-167**, 181-192.
20. M. P. Ruggeri, T. Selleri, I. Nova, E. Tronconi, J. A. Pihl, T. J. Toops and W. P. Partridge, *Top. Catal.*, 2016, **59**, 907-912.
21. M. P. Ruggeri, J. Luo, I. Nova, E. Tronconi, K. Kamasamudram and A. Yezerets, *Catal. Today*, 2018, **307**, 48-54.
22. I. Lezcano-Gonzalez, U. Deka, B. Arstad, A. Van Yperen-De Deyne, K. Hemelsoet, M. Waroquier, V. Van Speybroeck, B. M. Weckhuysen and A. M. Beale, *Phys. Chem. Chem. Phys.*, 2014, **16**, 1639-1650.
23. K. A. Lomachenko, E. Borfecchia, C. Negri, G. Berlier, C. Lamberti, P. Beato, H. Falsig and S. Bordiga, *J. Am. Chem. Soc.*, 2016, **138**, 12025-12028.
24. L. Chen, H. Falsig, T. V. W. Janssens, J. Jansson, M. Skoglundh and H. Grönbeck, *Catal. Sci. Technol.*, 2018, **8**, 2131-2136.
25. M. Colombo, I. Nova and E. Tronconi, *Catal. Today*, 2012, **197**, 243-255.
26. A. G. Greenaway, I. Lezcano-Gonzalez, M. Agote-Aran, E. K. Gibson, Y. Odarchenko and A. M. Beale, *Top. Catal.*, 2018, **61**, 175-182.
27. L. Chen, T. V. W. Janssens, M. Skoglundh and H. Grönbeck, *Top. Catal.*, 2018, **in press**, doi: 10.1007/s11244-11018-11095-y.
28. J. Y. Luo, F. Gao, K. Kamasamudram, N. Currier, C. H. F. Peden and A. Yezerets, *J. Catal.*, 2017, **348**, 291-299.
29. F. Gao, N. M. Washton, Y. L. Wang, M. Kollar, J. Szanyi and C. H. F. Peden, *J. Catal.*, 2015, **331**, 25-38.
30. K. Leistner, K. Xie, A. Kumar, K. Kamasamudram and L. Olsson, *Catal. Letter*, 2017, **147**, 1882-1890.
31. J. Jaumot, R. Gargallo, A. de Juan and R. Tauler, *Chemometrics Intell. Lab. Syst.*, 2005, **76**, 101-110.
32. J. Jaumot, A. de Juan and R. Tauler, *Chemometr. Intell. Lab.*, 2015, **140**, 1-12.
33. R. Tauler, *Chemometrics Intell. Lab. Syst.*, 1995, **30**, 133-146.
34. F. Giordanino, P. N. R. Vennestrom, L. F. Lundegaard, F. N. Stappen, S. L. Mossin, P. Beato, S. Bordiga and C. Lamberti, *Dalton Trans.*, 2013, **42**, 12741-12761.
35. F. Giordanino, E. Borfecchia, K. A. Lomachenko, A. Lazzarini, G. Agostini, E. Gallo, A. V. Soldatov, P. Beato, S. Bordiga and C. Lamberti, *J. Phys. Chem. Lett.*, 2014, **5**, 1552-1559.
36. A. Godiksen, F. N. Stappen, P. N. R. Vennestrom, F. Giordanino, S. B. Rasmussen, L. F. Lundegaard and S. Mossin, *J. Phys. Chem. C*, 2014, **118**, 23126-23138.
37. C. Andersen, M. Bremholm, P. Vennestrøm, A. Blichfeld, L. Lundegaard and I. B., *IUCrJ*, 2014, **1**, 382-386.
38. O. Mathon, A. Beteva, J. Borrel, D. Bugnazet, S. Gatla, R. Hino, I. Kantor, T. Mairs, M. Munoz, S. Pasternak, F. Perrin and S. Pascarelli, *J. Synchrotron Radiat.*, 2015, **22**, 1548-1554.
39. D. Bellet, B. Gorges, A. Dallery, P. Bernard, E. Pereiro and J. Baruchel, *J. Appl. Crystallogr.*, 2003, **36**, 366-367.
40. C. Lamberti, S. Bordiga, F. Bonino, C. Prestipino, G. Berlier, L. Capello, F. D'Acapito, F. Xamena and A. Zecchina, *Phys. Chem. Chem. Phys.*, 2003, **5**, 4502-4509.
41. S. Bordiga, E. Groppo, G. Agostini, J. A. van Bokhoven and C. Lamberti, *Chem. Rev.*, 2013, **113**, 1736-1850.
42. B. Ravel and M. Newville, *J. Synchrotron Radiat.*, 2005, **12**, 537-541.
43. C. Lamberti, G. Spoto, D. Scarano, C. Pazé, M. Salvalaggio, S. Bordiga, A. Zecchina, G. T. Palomino and F. Dacapito, *Chem. Phys. Lett.*, 1997, **269**, 500-508.
44. C. Prestipino, G. Berlier, F. Xamena, G. Spoto, S. Bordiga, A. Zecchina, G. T. Palomino, T. Yamamoto and C. Lamberti, *Chem. Phys. Lett.*, 2002, **363**, 389-396.
45. G. T. Palomino, P. Fisicaro, S. Bordiga, A. Zecchina, E. Giamello and C. Lamberti, *J. Phys. Chem. B*, 2000, **104**, 4064-4073.
46. F. X. Llabrés i Xamena, P. Fisicaro, G. Berlier, A. Zecchina, G. T. Palomino, C. Prestipino, S. Bordiga, E. Giamello and C. Lamberti, *J. Phys. Chem. B*, 2003, **107**, 7036-7044.
47. C. Lamberti, S. Bordiga, M. Salvalaggio, G. Spoto, A. Zecchina, F. Geobaldo, G. Vlaic and M. Bellatreccia, *J. Phys. Chem. B*, 1997, **101**, 344-360.
48. C. Lamberti, S. Bordiga, A. Zecchina, M. Salvalaggio, F. Geobaldo and C. O. Arean, *J. Chem. Soc.-Faraday Trans.*, 1998, **94**, 1519-1525.

49. K. A. Lomachenko, E. Borfecchia, S. Bordiga, A. V. Soldatov, P. Beato and C. Lamberti, *J. Phys.: Conf. Ser.*, 2016, **712**, 012041.
50. D. K. Pappas, A. Martini, M. Dyballa, K. Kvande, S. Teketel, K. A. Lomachenko, R. Baran, P. Glatzel, B. Arstad, G. Berlier, C. Lamberti, S. Bordiga, U. Olsbye, S. Svelle, P. Beato and E. Borfecchia, *J. Am. Chem. Soc.*, 2018, **140**, 15270-15278.
51. C. Barzan, A. Piovano, L. Braglia, G. A. Martino, C. Lamberti, S. Bordiga and E. Groppo, *J. Am. Chem. Soc.*, 2017, **139**, 17064-17073.
52. A. A. Guda, S. A. Guda, K. A. Lomachenko, M. A. Soldatov, I. A. Pankin, A. V. Soldatov, L. Braglia, A. L. Bugaev, A. Martini, M. Signorile, E. Groppo, A. Piovano, E. Borfecchia and C. Lamberti, *Catal. Today*, 2018, **in press**, doi: 10.1016/j.cattod.2018.10.071.
53. Freely downloadable at *http://www.mcrals.info/*.
54. W. Windig and J. Guilment, *Anal. Chem.*, 1991, **63**, 1425-1432.
55. C. Garino, E. Borfecchia, R. Gobetto, L. Salassa, J. A. van Bokhoven and C. Lamberti, *Coord. Chem. Rev.*, 2014, **277–278** 130-186.
56. E. I. Solomon, D. E. Heppner, E. M. Johnston, J. W. Ginsbach, J. Cirera, M. Qayyum, M. T. Kieber-Emmons, C. H. Kjaergaard, R. G. Hadt and L. Tian, *Chem. Rev.*, 2014, **114**, 3659-3853.
57. F. Gao and C. H. F. Peden, *Catalysts*, 2018, **8**, 140.
58. E. M. C. Alayon, M. Nachtegaal, A. Bodi and J. A. van Bokhoven, *ACS Catal.*, 2014, **4**, 16-22.
59. E. M. C. Alayon, M. Nachtegaal, A. Bodi, M. Ranocchiari and J. A. van Bokhoven, *Phys. Chem. Chem. Phys.*, 2015, **17**, 7681-7693.
60. V. L. Sushkevich, D. Palagin, M. Ranocchiari and J. A. van Bokhoven, *Science*, 2017, **356**, 523-527.
61. S. Grundner, M. A. C. Markovits, G. Li, M. Tromp, E. A. Pidko, E. J. M. Hensen, A. Jentys, M. Sanchez-Sanchez and J. A. Lercher, *Nat. Commun.*, 2015, **6**, 7546.
62. F. Göltl, P. Sautet and I. Hermans, *Catal. Today*, 2016, **267**, 41-46.
63. C. Paolucci, A. A. Verma, S. A. Bates, V. F. Kispersky, J. T. Miller, R. Gounder, W. N. Delgass, F. H. Ribeiro and W. F. Schneider, *Angew. Chem. Int. Ed.*, 2014, **53**, 11828-11833.
64. M. Lo Jacono, G. Fierro, R. Dragone, X. B. Feng, J. dItri and W. K. Hall, *J. Phys. Chem. B*, 1997, **101**, 1979-1984.
65. S. C. Larsen, A. Aylor, A. T. Bell and J. A. Reimer, *J. Phys. Chem.*, 1994, **98**, 11533-11540.
66. C. Paolucci, J. R. Di Iorio, F. H. Ribeiro, R. Gounder and W. F. Schneider, in *Advances in Catalysis*, ed. C. Song, Academic Press, 2016, vol. 59, pp. 1-107.
67. G. Lamble, A. Moen and D. G. Nicholson, *J. Chem. Soc. Farady Trans.*, 1994, **90**, 2211-2213.
68. R. Zhang, J. Szanyi, F. Gao and J.-S. McEwen, *Cat. Sci. Tech.*, 2016, **6**, 5812-5829.
69. L. S. Kau, D. J. Spira-Solomon, J. E. Pennerhahn, K. O. Hodgson and E. I. Solomon, *J. Am. Chem. Soc.*, 1987, **109**, 6433-6442.
70. M. L. Baker, M. W. Mara, J. J. Yan, K. O. Hodgson, B. Hedman and E. I. Solomon, *Coord. Chem. Rev.*, 2017, **345**, 182-208.
71. F. Gao, D. Mei, Y. Wang, J. Szanyi and C. H. F. Peden, *J. Am. Chem. Soc.*, 2017, **139**, 4935–4942.
72. G. Berlier, V. Crocellà, M. Signorile, E. Borfecchia, F. Bonino and S. Bordiga, in *Structure and Reactivity of Metals in Zeolite Materials*, eds. J. Pérez Pariente and M. Sánchez-Sánchez, Springer International Publishing, Cham, 2018, DOI: 10.1007/430_2018_24, pp. 91-154.
73. B. Ipek, M. J. Wulfers, H. Kim, F. Goltl, I. Hermans, J. P. Smith, K. S. Booksh, C. M. Brown and R. F. Lobo, *ACS Catal.*, 2017, **7**, 4291-4303.
74. B. E. R. Snyder, M. L. Bols, R. A. Schoonheydt, B. F. Sels and E. I. Solomon, *Chem. Rev.*, 2018, **118**, 2718-2768.
75. F. C. Jentoft, in *Advances in Catalysis*, Academic Press, 2009, vol. 52, pp. 129-211.
76. F. C. Meunier, *React. Chem. Eng.*, 2016, **1**, 134-141.
77. M. J. Wulfers, S. Teketel, B. Ipek and R. F. Lobo, *Chem. Commun.*, 2015, **51**, 4447-4450.
78. R. Oord, J. E. Schmidt and B. M. Weckhuysen, *Catal. Sci. Technol.*, 2018, **8**, 1028-1038.
79. L. N. Trevani, J. C. Roberts and P. R. Tremaine, *J. Solution Chem.*, 2001, **30**, 585-622.
80. J. A. Duffy, *J. Chem. Soc., Dalton Trans.*, 1983, 1475-1478.
81. A. B. P. Lever, *Inorganic electronic spectroscopy*, Elsevier Publishing Company, Amsterdam, 1968.
82. B. N. Figgis, *Introduction to Ligand Fields*, John Wiley & Sons Eds, New York, 1967.